 doi:10.20944/preprints202205.0377.v1

Article

Asymptotic Analysis of Detonation Development at SI Engine Conditions Using Computational Singular Perturbation

Iliana D. Dimitrova [1,2,*], Sangeeth Sanal [1], Minh Bau Luong [1], Efstathios-Al. Tingas [3,*], Hong G. Im [1,*]

[1] Clean Combustion Research Center (CCRC), Physical Sciences and Engineering Division, King Abdullah University of Science and Technology (KAUST), Thuwal 23955-6900, Saudi Arabia;
[2] Perth College, University of the Highlands and Islands (UHI), Crieff Rd., Perth PH1 2NX, United Kingdom;
[3] School of Engineering and the Built Environment (SEBE), Edinburgh Napier University (ENU), Edinburgh EH10 5DT, United Kingdom;
* Correspondence: e.tingas@napier.ac.uk (E.-A.T.); hong.im@kaust.edu.sa (H.G.I.)

Abstract: The occurrence and intensity of the detonation phenomenon at spark-ignition (SI) engine conditions is investigated, with the objective to successfully predict super-knock and to elucidate the effect of kinetics and transport at the ignition front. The computational singular perturbation (CSP) framework is employed in order to investigate the chemical and transport mechanisms of deflagration and detonation cases in the context of 2D high-fidelity numerical simulations. The analysis revealed that the detonation development is characterized by: (i) stronger explosive dynamics and (ii) enhanced role of convection. The role of chemistry was also found to be pivotal to the detonation development which explained the stronger explosive character of the system, the latter being an indication of the system's reactivity. The role of convection was found to be enhanced at the edge of the detonating front, thereby suggesting that it is the result and not the cause of the detonation onset. Moreover, the increased contribution of convection was found to be related mainly to heat convection. Remarkably, the detonation front was mainly characterized by dissipative and not explosive dynamics. Finally, diffusion was found to have negligible role to both examined cases.

Keywords: detonation; super-knock; CSP; explosive dynamics;

1. Introduction

Internal combustion engines (ICE) have been powering the transport industry for over a century and recent evidence suggests that they will remain the predominant mode powering the transport sector in a global scale for decades to come [1]. At the same time, the transport sector (hence ICEs) is a major contributor to greenhouse gases (GHG), contributing 14% to global CO_2 emissions, of which road transport consists 74% [2]. In addition, exhaust emissions such as NO_x, CO, HC, CO_2, SO_2, and particulate matter (PM) [3,4], can frequently cause illnesses in densely populated areas [5]. As a result, local governments all around the globe have been imposing strict regulations that aim to mitigate the adverse effects of ICEs. For instance, in 2021 the United Kingdom was the first major economy to ban all new gasoline and diesel passenger vehicles by 2030. Similar initiatives have also been undertaken by other countries such as Norway, Denmark and Japan, banning the sales of new diesel/gasoline vehicles by 2025, 2030 and 2035, respectively. On the other hand, countries like China and the USA do not currently have any plans for phasing out gasoline/diesel engine vehicles, however, they have all pledged to a net zero target by 2050 or 2060. Similarly, three of the world's biggest auto manufacturers, Toyota, Volkswagen, and the Nissan-Renault alliance, did not join the pledge of six major automakers, including Ford, Mercedes-Benz, General Motors and Volvo, to work toward phasing out sales of new gasoline and diesel-powered vehicles by 2035 in "leading markets" and by 2040 worldwide. This suggests that IC engines will maintain a large share in the global car market. To meet the increasing demands of lower carbon footprint, however, the current

 doi:10.20944/preprints202205.0377.v1

engine technology needs to be significantly improved in terms of both efficiency and emissions, with flexibility in fuels derived from petroleum or renewable sources.

One approach towards this direction is the downsized IC engines [6] that can produce comparable power of a larger engine through the use of different techniques: turbocharging or supercharging, often coupled with direct injection (DI), advanced exhaust gas recirculation (EGR) or variable valve timing (VVT). The main benefits from the downsized engines are the increased thermal and fuel efficiencies [7–11] and the inherent high-power density [12]. Downsized engines have been reported to mitigate successfully CO_2 emissions by reducing the fuel consumption [13,14], making it a serious contender in reducing greenhouse emissions and harmful pollutants [6,15]. Furthermore, the combustion at higher pressure potentially leads to fuel flexibility, as the variability in the fuel reactivity is reduced at elevated pressure.

One of the major technical challenges in downsized and boosted engines is the preignition and super-knock [9,16]. The phenomenon refers to a premature autoignition of the reactant mixture prior to the spark ignition due to various ignition sources [17–22], creating an reactant front propagation that may undergo deflagration-to-detonation (DDT) transition. This leads to intense pressure oscillations in the combustion chamber and create severe mechanical damage [23]. Optical diagnostics carried out by Wang et al. [16] showed that the mechanism of super-knock is described as hotspot-induced DDT followed by high-pressure oscillation. Detonation develops if there is a coherent coupling between the acoustic wave and the reaction front [24,25]. At these conditions, the front speed exceeds the Chapman-Jouguet detonation speed [26].

Considering its practical significance, many engineering strategies to suppress preignition and super-knock have been reported. Gong et al. [27] demonstrated a successful implementation of an early or late secondary injection, resulting in a decreased super-knock frequency, fuel consumption, and emissions, while NO_x level was found to be increased. Dai et al. [28] also reported that local NO_x concentrations play a role in detonation development in dimethyl ether (DME)/air mixtures within negative temperature coefficient (NTC) regime, in engines using EGR. Attenuation of fuel reactivity was also considered. Liu et al. [29] performed experiments with rapid compression machine (RCM), where replacing part of gasoline fuel with less reactive methane or propane was found to transition the combustion mode from detonation to flame propagation. They also reported that methanol was effective in suppressing the detonation development. The effect of spark location and timing were also found to have an impact [30], such that advancing the spark timing was found to induce super-knock at high compression ratio conditions [26,31,32].

Fundamental description of the ignition and detonation development has also been studied extensively. Since theoretical classification of ignition regimes by Zeldovich [24], Bradley and coworkers [17,33–35] proposed the regime diagram to identify the detonation propensity in terms of two nondimensional parameters based on the reactivity of the mixture and the temperature distribution in the hot spot. A number of one-dimensional simulations were conducted to reproduce the "detonation peninsula" for a specific choice of fuels [36–45]. Sow et al. [46] also reported that the temperature gradient in the bulk mixture affects the run-up time and intensity of the detonation. Luong et al. [47,48] extended the theory into multidimensional direct numerical simulations to characterize the ignition behavior in terms of turbulence intensity and temperature fluctuations in a statistical context.

While considerable fundamental insights have been obtained to predict the critical condition at the onset of the detonation development, the dynamics of the phenomena, such as the interplay between the relevant transport processes and dominant chemical pathways are of interest in universal understanding of the complex phenomena. To this end, a mathematical theory that considers the dynamical features of the system serves as a systematic analytical tool.

Based on the geometric singular perturbation (GSP) concept introduced in the 1970s [49–51], the computational singular perturbation (CSP) is an algorithmic asymptotic analy-

 doi:10.20944/preprints202205.0377.v1

sis developed by Lam and Goussis [52,53], initially applied in problems of chemical kinetics [54–56] and later extended to other fields, such as reacting flows [57–61], biology [62–66], metabolic networks [67–69], pharmacokinetics [70,71] and others. In problems of reacting flows with detailed chemistry, CSP allows a characterization of dynamical structures and their properties in the phase space, by identifying the fastest timescales that become quickly exhausted to equilibrium, thus establishing certain constraints called slow invariant manifolds (SIM), on which the system dynamics evolve at fast and slow active timescales. The simplified form of the governing equations produces the reduced model, which governs the flow along the SIM. In addition, various mathematical formulas were developed to identify the important reactions that contribute to the mode amplitude or the time scales, in order to provide physical interpretation of the phenomena.

The objective of this study is to apply the CSP algorithm and various tools in order to identify key changes in the system's dynamics and to examine the interplay between transport processes (convective and diffusive) and chemistry towards the development of detonation phenomena. The results from this examination aim to inform the development of future algorithms, potentially related to machine learning, that will be used for the prediction of detonation events in SI engines. The analysis is based on data produced by two-dimensional simulations representing engine conditions, investigated under two distinguished conditions with and without detonation occurrence.

2. Material and Methods

2.1. Numerical Setup

CONVERGE software was utilized for simulating two 2D cases, representative of SI engine conditions, carried out on Shaheen II supercomputer at KAUST. The CFD software is widely used for engine applications with the capability to capture detonation phenomena [30,47,72–75]. To integrate in time the fully compressible Navier-Stokes, energy and species equations, a pressure-implicit with splitting of operator (PISO) algorithm is used, involving a predictor and two corrector steps, computing the pressure and velocity terms. High resolution simulations were run in the direct numerical simulation (DNS) mode without turbulence submodels, with detailed chemical reaction terms solved by the SAGE subroutine [76], fully coupled with the flow solver. The time integration is performed with a variable time step, with Δt_{min} ranging from 5e-10 to 5e-09 s. For the boundary conditions, the four boundaries are represented as solid walls at which no-slip velocity and zero-gradient conditions for scalar variables are imposed. The spatial discretization is handled by the monotonic upstream-centred scheme for conservation laws (MUSCL) scheme, providing a 2^{nd} order of accuracy for the convection term. In all cases, a square 2D domain was employed with dimensions of 20.464×20.464 mm. The domain is made up of a base grid of size of 32 μm with level 2 adaptive mesh refinement (AMR) computed at every timestep, yielding the minimum grid size of 8 μm. As shown in Table 1, a single Gaussian hot spot representing the spark plug in an SI engine is imposed at the center of the left domain boundary with distribution σ = 1 mm, and its resolution is further improved by setting up a level 3 fixed embedding (FE) over it, at r = 5 mm, yielding a local cell refinement of 4 μm. The hot spot maximum temperature is set at T_{max} = 1400 K, representing practical engine conditions. Two cases were considered; Case A is representative of detonation (supersonic behaviour), while Case B is a representative of deflagration (subsonic behaviour).

Figure 1 displays the mesh resolution at the initial timestep (a), t_0, for both cases, and at the timestep of 99% τ_{ign} for Cases A and B ((b) and (c)). It is shown that the grid refinement increases significantly in the areas of high temperature gradients. At the very initial timestep, this area is near the hotspot, while as time evolves autoigniting kernels emerge and the AMR algorithm adds the grid refinement accordingly.

Preprints (www.preprints.org) | NOT PEER-REVIEWED | Posted: 27 May 2022 doi:10.20944/preprints202205.0377.v1

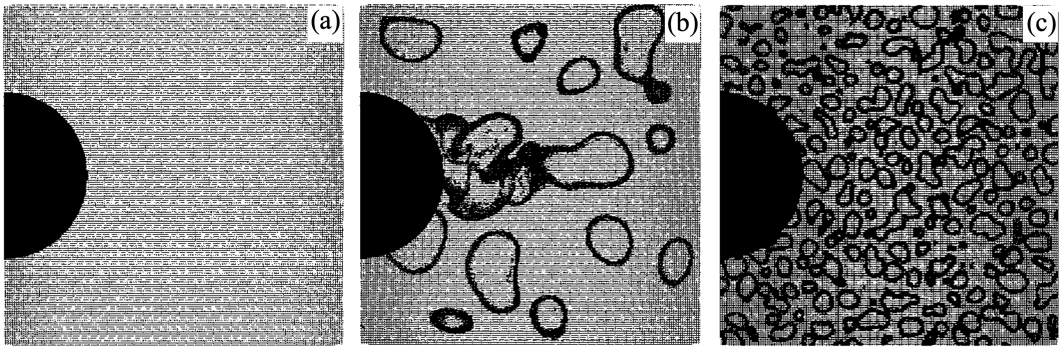

Figure 1. Grid resolution after AMR and FE refinement at (a) t_0 for both Cases A and B, (b) 99% τ_{ign} for Case A and (c) 99% τ_{ign} for Case B.

In addition, the inherent temperature inhomogeneity found in IC engines was addressed by imposing a temperature stratification in the mixture of uniform composition as the initial condition, as shown in Fig. 2. The most energetic length scale of temperature fluctuation, l_T, is 5 mm and 1.5 mm for Cases A and B, respectively, and the temperature fluctuations in the domain were imposed by the root mean square (RMS) temperature ΔT_{RMS} = 5 K.

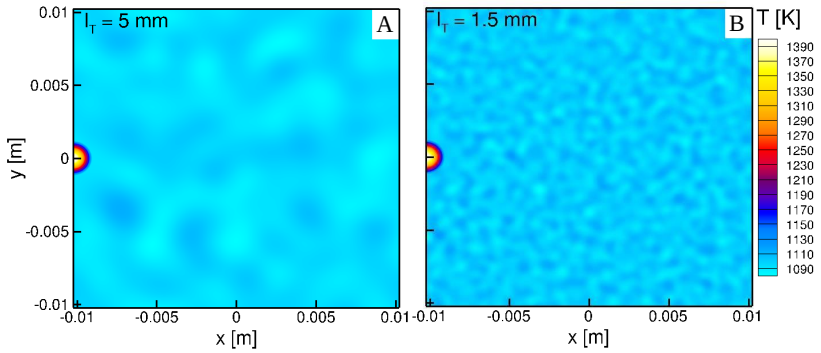

Figure 2. Temperature fields for Case A (left) and Case B (right) at the initial timestep t_0.

Table 1. Summary of the numerical setup.

Simulation Setup	Characteristics
Domain	20.464 x 20.464 mm
Grid	32 x 32 μm, AMR level 2
Gaussian hotspot	T_{max} = 1400 K, σ= 1 mm, Fixed Embedding scale 3, r = 5 mm
Temperature field	T_{mean} = 1100 K, ΔT_{RMS} = 5 K, l_T = 5 mm, 1.5 mm
Pressure	P_{in} = 35 atm
Reactive fuel	C_2H_5OH, φ = 1
Chemical mechanism	40 species, 180 elementary reactions

The initial pressure, P_{in} in both cases was set at 35 atm, representing the case of the in-cylinder pressure at the top dead centre (TDC), while the von Neumann pressure P_{ZND} based on the initial mean temperature is 34.8 MPa, and the Chapman-Jouguet velocity U_{CJ} is 1834.2 m/s. Ethanol is chosen as a fuel because it is considered to be a representative non-NTC related renewable biodiesel. Additionally, due to the high autoignitive resistance provided by the high octane number (ON) of ethanol, triggering detonation in such conditions is physically harder. Therefore, the results of this study is applicable to fuels/blends at higher ON ratings. The chemical mechanism consists of 40

 doi:10.20944/preprints202205.0377.v1

species and 180 elementary reactions [77]. The equivalence ratio of the bulk mixture is initially set to $\varphi = 1$. The strong detonation case (Case A) and the deflagration case (Case B) both have a mean temperature of 1100 K. The high bulk mixture temperatures of both cases aim to reflect the end gas autoignition conditions in order to reduce the computational cost, following the practice of Luong et al. [73,74]. A good balance between computational expenses and fidelity is achieved.

2.2. Ignition regime characterization

The Bradley ignition regime diagram was developed on the basis of one-dimensional setup, but serves as a representative metric for the 2D simulations. The Bradley diagram employs two non-dimensional numbers, (ξ and ε), to identify the developing detonation peninsula, thus distinguishing the zones of subsonic and supersonic autoignitive fronts, as well as thermal explosion [35]. The ξ parameter represents the ratio of the speed of sound (a) to the propagation speed (S_{sp}).

$$\xi = a/S_{sp} \tag{1}$$

Note that the upper and lower ξ limits of the C-shaped curve of the the developing detonation regime strongly depend on the initial conditions, fuel types, and the kinetic model used in simulations [41,42]. In general, a strong detonation development is expected when ξ ranges between 1 to $O(10)$ [41,42], and for ξ values lower than unity homogeneous thermal explosion occurs.

The ε parameter denotes the ratio of the residence time of the pressure wave in the radius of the autoignition kernel (r_{hs}) to the excitation time (τ_e):

$$\varepsilon = (r_{hs}/a)/\tau_e \tag{2}$$

where τ_e is determined from the heat release rate profile at the reference mixture condition [35].

In multi-dimentional problems, the representative ξ in a uniform mixture with temperature inhomogeneities is approximated as $\xi \cong a\left|d\tau_{ign}/dT\right|\left|\widetilde{\nabla T}\right|$ [48,73,74,78–80] where $\widetilde{\nabla T}$ is the statistical mean temperature gradient. In the isotropic temperature field fluctuations, Peters et al. [81] found that the characteristic length scale representing the size of hot spots r_{hs} is comparable with the mean distance of the dissipation elements, $\bar{l}_{DE}$. As such, $\widetilde{\nabla T}$ is approximated as $\widetilde{\nabla T} \cong T_{RMS}/\bar{l}_{DE}$. $\bar{l}_{DE}$ is found to be approximately equal to a half of the two-point autocorrelation integral length scale, $\bar{l}_{DE} \cong l_{et}/2$, for the isotropic energy spectrum adopted in this study [48].

Similarly, ε for the multidimensional field is approximated as [48]

$$\varepsilon = \bar{l}_{DE}/(l_m/\alpha)\,, \tag{3}$$

where l_m is the minimum runup distance to form direct detonation initiation from a hot spot [82]. α is the weighting factor, $\alpha = 4$, that accounts for the shortened runup distance of detonation formation quantitatively observed in the DNS, resulting from the interaction and collision of multiple ignition fronts in the highly-reactive transient mixture conditions.

The significance of ξ and ε is that no detonation is expected for $\varepsilon \ll 1$ regardless of the magnitude of the ξ parameter. As ε approaches unity, the transient mixture state shifts towards the boundary of the detonation peninsula, and the developing detonation is expected. For $\varepsilon \gg 1$ fully developed detonation is expected to occur for $\xi \sim 1$ to $O(10)$ [48].

In this study, it was found that $\varepsilon = 1.3$ and $\xi = 9.3$ for Case A, and $\varepsilon = 0.4$ and $\xi = 31$ for Case B, thereby suggesting that Case A exhibits strong detonation as opposed to the non-detonating (deflagrative) Case B.

Preprints (www.preprints.org) | NOT PEER-REVIEWED | Posted: 27 May 2022 doi:10.20944/preprints202205.0377.v1

2.3. Computational singular perturbation (CSP) and its algorithmic tools

The details of the CSP method used herein and its algorithmic tools have been discussed elsewhere (see for instance [83–87]), and only a brief summary is provided here. Consider the system of species and temperature equations in the general form of

$$\frac{\partial \mathbf{z}}{\partial t} = \mathbf{L}_T(\mathbf{z}) + \mathbf{g}(\mathbf{z}), \qquad \mathbf{L}_T(\mathbf{z}) = \mathbf{L}_C(\mathbf{z}) + \mathbf{L}_D(\mathbf{z}) \tag{4}$$

where $\mathbf{z}$ the system's $(N+1)$ state vector that includes the N mass fractions ($\mathbf{y}$) and temperature (T), $\mathbf{L}_D(\mathbf{z})$, $\mathbf{L}_C(\mathbf{z})$, $\mathbf{L}_T(\mathbf{z})$ the spatial transport operators denoting diffusion, convection and their sum, respectively, and $\mathbf{g}(\mathbf{z})$ the chemical source term. In the absence of any spatial inhomogeneities (i.e., $\mathbf{L}_T(\mathbf{z}) = \mathbf{0}$) Eq. 4 degenerates to:

$$\frac{\partial \mathbf{z}}{\partial t} = \mathbf{g}(\mathbf{z}), \qquad \mathbf{L}_T(\mathbf{z}) = \mathbf{0} \tag{5}$$

According to the CSP framework, the system of Eq. 4 can be transformed to []:

$$\frac{\partial \mathbf{z}}{\partial t} = \sum_{i=1}^{N+1} \boldsymbol{a}_i h^i, \qquad h^i = \boldsymbol{b}^i(\boldsymbol{L}_T + \boldsymbol{g}) \tag{6}$$

where $\boldsymbol{a}_i$, $\boldsymbol{b}^i$ the i-th dual (row and column, respectively) CSP basis vectors, so that $\boldsymbol{b}^j \boldsymbol{a}_i = \delta_i^j$. In essence, CSP allows us to decompose the state vector to a set of $(N+1)$ CSP modes. Each CSP mode is characterized by a timescale τ_i and an amplitude h^i; the former dictates the frame of action of the i-th mode, while the latter defines its impact to the system's slow evolution [88,89]. When M (fast) modes become exhausted, the system is confined to evolve on a slow invariant manifold (SIM) under the action of the remaining $\big((N+1)-M\big)$ slow (active) ones, and the reduced model can be obtained:

$$\frac{\partial \mathbf{z}}{\partial t} \approx \sum_{i=M}^{N+1} \boldsymbol{a}_i h^i, \qquad h^j \approx 0, j = 1, ...M \tag{7}$$

For leading order accuracy, the CSP basis vectors $\boldsymbol{a}_i$, $\boldsymbol{b}^i$ can be approximated by the right and left eigenvectors $\boldsymbol{\alpha}_i$, $\boldsymbol{\beta}^i$, respectively, of the Jacobian J of the chemical source term $\boldsymbol{g}(\boldsymbol{z})$ [90–92]. Then, the i-th timescale τ_i can be calculated on the basis of the respective eigenvalue λ_i, i.e., $\tau_i = \frac{1}{|\lambda_i|}$. The sign of the eigenvalue (positive or negative) determines the nature of the respective CSP mode; a negative eigenvalue indicates a *dissipative* mode that tends to drive the system towards equilibrium, while a positive eigenvalue is called *explosive* [2,93,94] that drives the system away from the equilibrium. *Explosive* modes have been extensively investigated in reacting flows because they are inherently related to limit phenomena and flames [95–97]. As previously discussed, however, their mere existence does not qualify them as dominant ones for the system's slow evolution. In fact, their action may be largely cancelled by the action of other more active dissipative modes, hence their net effect can be insignificant. In any case, their consideration as dominant ones has to always be subject to investigation. In fact, according to Eq. 7, two conditions must be satisfied in order for a mode to have a strong effect on the system's slow evolution [98,99]: (i) its timescale τ_i must be among the fastest of the slow ones, i.e., $\tau_{M+1} \leq \tau_i \leq \tau_{M+k}$, where $k > 1$ but sufficiently small, and (ii) its amplitude h^i must be the largest one in magnitude (or at least sufficiently close to the largest one).

To assess the contribution of each physical process (chemical or transport-related) to the development of the i-th amplitude h^i, the amplitude participation index (API) is used [59]. For a chemical source term expressed as

$$\boldsymbol{g}(\boldsymbol{z}) = \sum_{k=1}^{2K} \hat{\boldsymbol{S}}_k R^k \tag{8}$$

Preprints (www.preprints.org) | NOT PEER-REVIEWED | Posted: 27 May 2022 doi:10.20944/preprints202205.0377.v1

where $\hat{\boldsymbol{S}}_k$ the generalized stoichiometric vector of the k-th reaction, R^k the respective reaction rate and $2K$ the total number of unidirectional reactions, the amplitude h^i is written in the form [100]:

$$h^i = \boldsymbol{\beta}^i(\boldsymbol{L}_T + \boldsymbol{g}) = \sum_{j=1}^{N+1} \beta_j^i L_{T,j} + \sum_{k=1}^{2K} \boldsymbol{\beta}^i \hat{\boldsymbol{S}}_k R^k = \sum_{m=1}^{2K+N+1} \gamma_m^i \tag{9}$$

Then, the API is defined as:

$$P_k^n = \frac{\gamma_k^n}{\sum_{m=1}^{2K+N+1} |\gamma_m^n|} \tag{10}$$

thereby measuring the contribution of the k-th process to the n-th CSP mode [101,102]. The signs of the eigenvectors $\boldsymbol{\alpha}_i$, $\boldsymbol{\beta}_i$ are properly adapted in order to ensure that the amplitudes of all slow (active) modes are positive. The positive API values then indicate that the associated processes enhance the impact of the respective mode while the opposite holds for negative API values [103,104].

An additional tool recently developed in the CSP framework is the tangential stretching rate (TSR) [105–108], which is the resultant effect of all eigenvalues with weights that depend on the amplitudes of the modes, i.e.,

$$\omega_{\tilde{\tau}_{R+T}} = \sum_{i=M+1}^{N+1} W_{i,R+T}\lambda_i, \qquad W_{i,R+T} = \frac{h^i}{L_T + g} \sum_{k=M+1}^{N+1} \frac{h^k}{L_T + g} \tag{11}$$

where L_T and g the norms of $\boldsymbol{L}_T$ and $\boldsymbol{g}$, respectively. In the absence of any spatial inhomogeneities, Eq. 11 degenerates to:

$$\omega_{\tilde{\tau}_R} = \sum_{i=M+1}^{N+1} W_{i,R}\lambda_i, \qquad W_{i,R} = \frac{h^i}{g} \sum_{k=M+1}^{N+1} \frac{h^k}{g} \tag{12}$$

Note that in the above definition TSR only considers the action of the slow (active) modes.

As such, the TSR on the basis of Eq. 11 is called *reactive-transport TSR* while that from Eq. 12 is *reactive TSR*, to reflect the presence or absence of the transport process in the formulation [109,110]. Furthermore, due to the large dynamic range of values that both $\omega_{\tilde{\tau}_{R+T}}$ and $\omega_{\tilde{\tau}_R}$ obtain, they are both represented in logarithms, i.e.:

$$\Omega_{R+T} = Sign(\omega_{\tilde{\tau}_{R+T}}) \cdot Log_{10}|\omega_{\tilde{\tau}_{R+T}}|, \qquad \Omega_R = Sign(\omega_{\tilde{\tau}_R}) \cdot Log_{10}|\omega_{\tilde{\tau}_R}| \tag{13}$$

In the following analysis, the system's fast explosive eigenvalue is similarly logarithmically scaled, i.e., $\Lambda_{e,f} = Log_{10}\lambda_{e,f}$. To avoid clutters, values of $\omega_{\tilde{\tau}_{R+T}}$, $\omega_{\tilde{\tau}_R}$ and $\lambda_{e,f}$ less than unity are not presented because they bear little impact on the system's slow dynamics. Hence, positive and negative values of Ω_{R+T} and Ω_R denote explosive and dissipative behavior. All physical timescales are normalized by a nominal time of 1 second, such that the magnitudes shown in the results are non-dimensional.

By definition, $\Omega_{R+T} \approx \Omega_R$ implies that the system becomes nearly homogeneous, hence the chemical reactions dominate the system dynamics. However, when $\Omega_{R+T} \neq \Omega_R$, no simple conclusion can be drawn for the relative significance of the transport and chemical reactions. In that case, an alternative approach is required, and the TSR amplitude participation index (TSR-API) provides valuable insights. The TSR-API is a weighted average of the API values of the k-th process from all active modes with weights that depend on the contribution of each mode to the construction of TSR, i.e.

$$H_k^{R+T} = \boldsymbol{V}^{R+T}\boldsymbol{API}_k \tag{14}$$

Preprints (www.preprints.org) | NOT PEER-REVIEWED | Posted: 27 May 2022 doi:10.20944/preprints202205.0377.v1

where $\boldsymbol{V}^{R+T}$ a $((N+1)-M)$ row vector which contains the weights of all active modes to $\omega_{\tilde{\tau}_{R+T}}$, i.e.,

$$V_n^{R+T} = Sign(Re(\lambda_n)) \cdot \frac{W_{n,R+T}|\lambda_n|}{\sum_{i=M+1}^{N+1} |W_{i,R+T}|\lambda_i||} \tag{15}$$

and $\boldsymbol{API}_k$ a $((N+1)-M)$ column vector containing the API values P_k^n of the k-th process across all n active modes, $(n = M+1, ..., N+1)$. Since the TSR-API tool H_k^{R+T} is defined for both chemical reactions and transport-related processes, both effects are aggregated to obtain the net contribution of chemistry and transport to the magnitude and nature (dissipative or explosive) of the TSR ($\omega_{\tilde{\tau}_{R+T}}$), i.e.:

$$H_R^{R+T} = \sum_{k=1}^{2K} H_k^{R+T}, H_D^{R+T} = \sum_{k=1}^{N+1} H_k^{R+T}, H_C^{R+T} = \sum_{k=1}^{N+1} H_k^{R+T}, H_T^{R+T} = \sum_{k=1}^{2(N+1)} H_k^{R+T} \tag{16}$$

In the above Eq. 16, H_R^{R+T}, H_D^{R+T}, H_C^{R+T}, H_T^{R+T} denote the overall contributions of chemistry, diffusion, convection and transport (i.e., both convection and diffusion), respectively, to $\omega_{\tilde{\tau}_{R+T}}$.

In the following, for all presented results related to the CSP analysis, the CSPTk package [106,111,112] integrated with the TChem [113] package for thermo-kinetic database management was employed.

3. Results and discussion

3.1. Overall combustion characteristics

To properly analyze the ignition dynamics of two distinct Cases A and B, which exhibit the detonation development and regular deflagration, respectively, instantaneous data fields at comparable stages were selected for analysis in order to compare the evolution characteristics in both cases. Scaling the temporal evolution of both systems against the respective ignition delay times (determined on the basis of the maximum rate of change of the mean temperature), five instants (t_1-t_5) were selected as shown in Table 2.

Table 2. Timestep selection for Case A and Case B .

Timestep		Case A			Case B		
		t [ms]	P_{max}/P_{ZND}	T_{mean} [K]	t [ms]	P_{max}/P_{ZND}	T_{mean} [K]
t_1	$0.975\tau_{ign}$	0.21999	0.16	1,386.9	0.22167	0.15	1,441.9
t_2	$0.980\tau_{ign}$	0.22112	0.32	1,468.7	0.22281	0.17	1,519.1
t_3	$0.988\tau_{ign}$	0.22292	0.96	1,620.4	0.22463	0.21	1,714.6
t_4	$0.990\tau_{ign}$	0.22337	1.26	1,692.9	0.22508	0.25	1,789.3
t_5	$1.000\tau_{ign}$	0.22563	3.37	2,463.9	0.22736	0.65	2.526.7

Figure 3 shows that the selected instants capture the critical moments as both the mean pressure and temperature evolve significantly during the ignition. In addition, for the detonating case, Case A, the first three instants are before the detonation onset, t_4 is immediately after the detonation onset and at t_5 the detonation event has evolved further. A time is referred to as "*before*" or "*after*" the detonation onset based on whether the local pressure normalized by the von Neumann pressure (P_{ZND}) is less or greater than unity. Considering that P_{ZND} = 34.8 MPa for both cases, Fig. 3 shows that P_{max} of Case A clearly exceeds P_{ZND}, reaching P_{max}/P_{ZND} values of 9.7. In fact, at t_3 the pressure ratio is just below unity (value of 0.96) while at t_4 it has just become greater than unity (value of 1.26), and at t_5 it has increased further to 3.37. As will be shown next, the P_{max} values detailed in Table 2 and Fig. 3 all relate to the same ignition kernel. On the contrary, the pressure of Case B does not exceed P_{ZND}, $P_{max}/P_{ZND} < 1$.

To further assess the detonability of Case A, the temperature field at five selected instants are shown in Fig. 4. A notable difference between the two cases is the significantly larger number of ignition kernels established in Case B, which is a direct consequence of

Preprints (www.preprints.org) | NOT PEER-REVIEWED | Posted: 27 May 2022 doi:10.20944/preprints202205.0377.v1

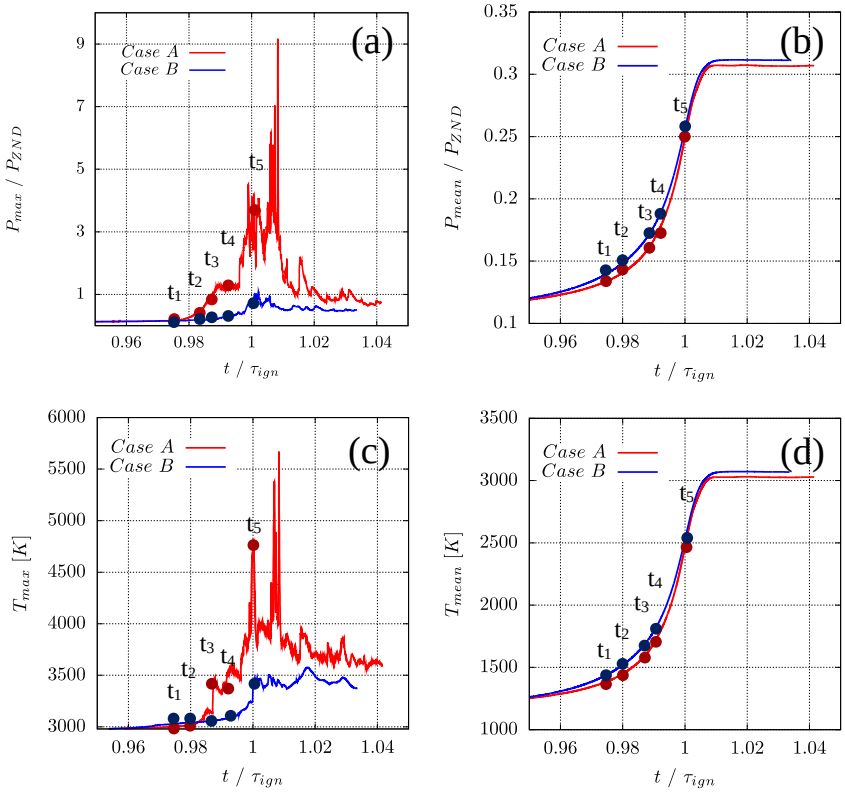

Figure 3. (a) Normalized maximum pressure, (b) Normalized mean pressure; (c) Maximum temperature, (d) Mean temperature. Red lines and markers denote Case A, blue lines and markers denote Case B. The respective values for Cases A and B are marked for the five time selections. For the exact values of the highlighted instants see Table 2.

the smaller l_T of Case B compared to Case A (1.5 mm and 5.0 mm, respectively). Hence, in Case A larger high-temperature spots allow a longer run-up distance to develop detonation, resulting in favorable conditions for detonation [114]. On the other hand, in Case B the smaller l_T leads to a larger number of smaller pockets of gases that autoignite concurrently. This results in less energetic, smaller spots unable to develop into detonation due to their competition with the consumption of the unburned fuel.

Fig. 4 shows that the ignition kernels created in Case A develop further in time and undergo collision and merging, thereby establishing new and stronger ignition fronts. The merging of ignition fronts directly results in strengthening the associated pressure waves. Closed-up views in Fig. 5 clearly show that the detonation onset in Case A is a consequence of the shock-to-shock interaction among at least three ignition kernels which appear to merge at t_3 and induce detonation development as manifested by the high pressure ratio (P/P_{ZND}) achieved at t_4. On the other hand, in Case B, the merging of the ignition kernels does not affect the pressure waves which remain uncoupled from the ignition propagation fronts, hence no noticeable detonation occurs.

3.2. Computational singular perturbation (CSP) analysis

Having examined the physical characteristics of pressure and temperature fields, the next step is to examine the dynamics of the system in both cases, in view of the CSP diagnostics and particularly Ω_R, Ω_{R+T} and $\Lambda_{e,f}$. Recall that Ω_R and Ω_{R+T} can take both positive (explosive) and negative (dissipative) values, while $\Lambda_{e,f}$ by definition takes only positive values and indicates explosive dynamics. As a result, Ω_R and Ω_{R+T} are defined everywhere in the computational domain, whereas $\Lambda_{e,f}$ only exists in certain parts of the

Preprints (www.preprints.org) | NOT PEER-REVIEWED | Posted: 27 May 2022 doi:10.20944/preprints202205.0377.v1

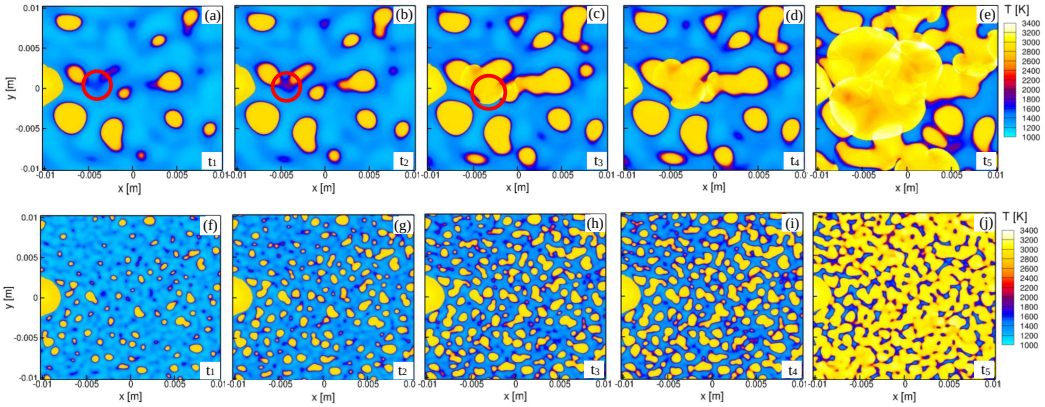

Figure 4. Temporal evolution of temperature contours for the five selected times for Case A (first row) and B (second row). In subfigures a–c of Case A, the red circle indicates the location where the detonation event is first established. For the details of the selected times see Table 2 and Fig. 3.

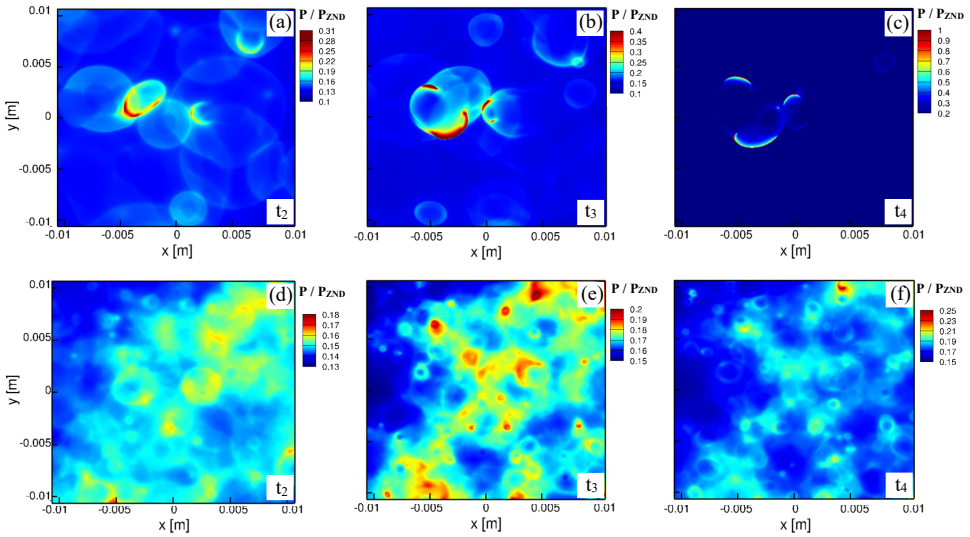

Figure 5. Temporal evolution of the normalized (against P_{ZND}) pressure for Case A (upper row) and B (lower row), for three selected times, t_2-t_4. For the details of the selected times see Table 2 and Fig. 3.

domain. This is confirmed in Fig. 6 which shows the spatial distributions of Ω_R, Ω_{R+T} and $\Lambda_{e,f}$ for both cases at t_4, i.e., the instants of the detonation onset for Case 4.

Comparing Ω_R and Ω_{R+T} in both cases, it is first noted that hardly any qualitative and quantitative differences are observed. As will be discussed next, this is a misleading observation, since in some key locations they do exhibit notable differences and it is these locations that contribute the most to the detonation development.

Second, $\Lambda_{e,f}$ appears to exist in a wider region of the computational domain in contrast to Ω_R and Ω_{R+T} which become positive (hence suggesting explosive dynamics) at a much smaller fraction of the computational domain. The difference between $\Lambda_{e,f}$ and Ω_{R+T} is more clearly highlighted in subfigures 6(d) and (h) where the positive Ω_{R+T} regions (color) are overlaid on positive $\Lambda_{e,f}$ regions (black and white). It is evident that positive $\Lambda_{e,f}$ does not always represent the explosive nature of the system's dynamics, since its action is cancelled by that of more active dissipative mode(s). Only a smaller subset of positive Ω_{R+T} regions are considered truly explosive. Hence, the diagostics solely based on $\Lambda_{e,f}$ may lead to an erroneous interpretation of the explosion characteristics, thereby rendering the drawn conclusions, in the best case, questionable [115–122]. This is in agreement with earlier work in turbulent and MILD combustion that reached the same conclusion and

Preprints (www.preprints.org) | NOT PEER-REVIEWED | Posted: 27 May 2022 doi:10.20944/preprints202205.0377.v1

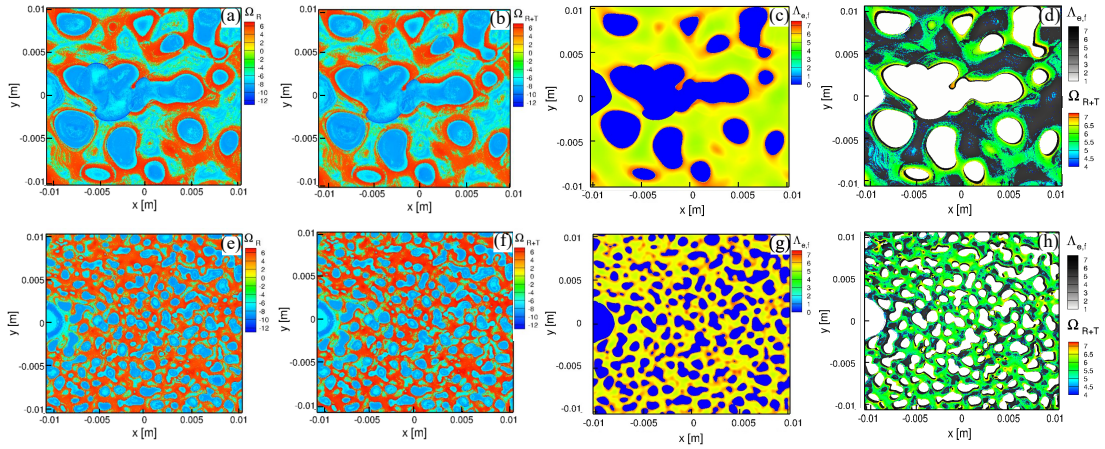

Figure 6. Results for Cases A (a - d) and B (e - h) at t_4. From left to right, spatial distributions of Ω_R (a, e), Ω_{R+T} (b, f), $\Lambda_{e,f}$ (c, g) and $\Lambda_{e,f}$ overlaid with $\Omega_{R+T} > 0$ (d, h).

highlighted that $\Lambda_{e,f}$ can compete with dissipative modes which become more active (i.e., faster in terms of their timescales and stronger in terms of their amplitudes), hence the *a priori* use of solely $\Lambda_{e,f}$ for the characterisation of the system's dynamics is inappropriate [109,110,123,124].

Another observation from comparing Fig. 6 and Fig. 4 is that Ω_R, Ω_{R+T} and $\Lambda_{e,f}$ all become negative (or undefined in the case of $\Lambda_{e,f}$) in the regions where the fuel has been consumed and the temperature is high. However, the converse holds true only for $\Lambda_{e,f}$ but not for Ω_R and Ω_{R+T}, that is, regions of unburned mixture and low temperature are not always associated with positive values of Ω_R and Ω_{R+T}. Finally, the energetic length scale of temperature (l_T) in Case B directly impacts the spatial distribution of Ω_R, Ω_{R+T} and $\Lambda_{e,f}$.

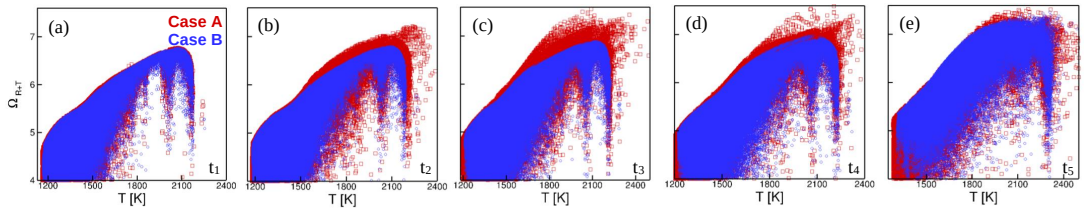

Figure 7. Scatter plots of Ω_{R+T} against temperature, for Cases A and B, at the five selected times. For the details of the selected times, see Table 2 and Fig. 3.

The relation between Ω_{R+T} and temperature is examined further in Fig. 7 which compares the highly positive values of Ω_{R+T} against temperature for both cases at the five selected times in the form of scatter plots. At t_1, the two cases exhibit minor differences and reach the same maximum values. At t_2, however, a noticeable difference in the maximum Ω_{R+T} values becomes apparent, with Case A obtaining higher Ω_{R+T} values than Case B. At t_3, when Case A is just before the knock onset, the difference between the two cases becomes more pronounced and Ω_{R+T} obtains even higher values than those obtained at t_2. At t_4, Case A has just passed the detonation onset and the difference in the high Ω_{R+T} values between the two cases becomes attenuated. Eventually, at t_5 the two cases look very similar in terms of their highest Ω_{R+T} values.

These results indicate that the detonation development is manifested by the highest Ω_{R+T} mostly prior to the event (i.e., t_2, t_3) and remains visible immediately after the detonation occurrence at t_4. In fact, a careful examination of the data revealed that Ω_{R+T} in Case A is higher than that in Case B only within the ignition kernels where the detonation develops. This is a significant finding, indicating that the detonation development can be accurately predicted using the appropriate CSP tools. The finding is intuitive because

Preprints (www.preprints.org) | NOT PEER-REVIEWED | Posted: 27 May 2022 doi:10.20944/preprints202205.0377.v1

detonation is a result of the positive feedback between the heat release in the ignition front and the pressure wave. The TSR metric serves as an unambiguous marker for the resultant explosive dynamics.

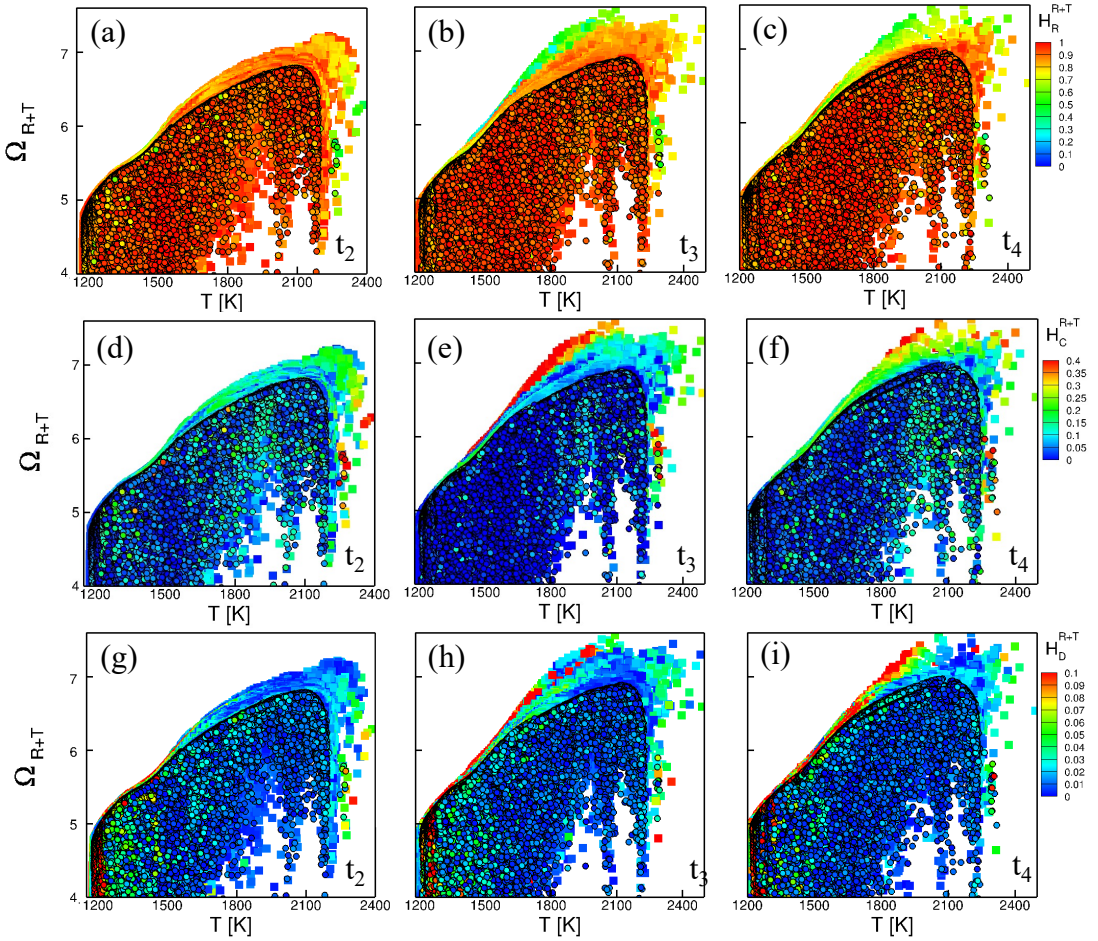

Figure 8. Scatter plots of Ω_{R+T} against temperature, for Cases A and B, at three selected times (t_2-t_4), where each cell has been colored based on the contribution of chemical reactions (a - c), convection (d - f) and diffusion (g - i). For the details of the selected times, see Table 2 and Fig. 3.

Having identified Ω_{R+T} as a proper metric to predict detonation, the next question is about the role of transport relative to chemical reactions in driving the explosive dynamics. Figure 8 shows scatter plots of Ω_{R+T} against temperature as shown in Fig. 7, but the data points are colored according to the TSR-API, i.e., contribution of chemistry (subfigures a-c), convection (d-f) and diffusion (g-i) for Cases A (square symbols) and B (circle symbols with solid edges), at three selected times (t_2-t_4). First, the results indicate that chemical reactions indeed play the most important role for both cases at all times. However, note that the data points where Ω_{R+T} in Case A exceeds that in Case B are characterized by the increased role of transport processes, especially convection. This is manifested at all times but it becomes more pronounced as the detonation onset is approached (at t_3). Immediately after the detonation onset, the increased role of the transport processes becomes attenuated. Moreover, the points that extend the explosive dynamics to higher temperatures in Case A are also characterized by the increased role of transport and particularly of convection. On the other hand, the highest contribution of convection is also seen at low and intermediate temperatures (see t_2 in Fig. 8). Diffusion also appears to have its role increased in the detonating case, but its contribution is relatively small compared to that of convection.

Preprints (www.preprints.org) | NOT PEER-REVIEWED | Posted: 27 May 2022 doi:10.20944/preprints202205.0377.v1

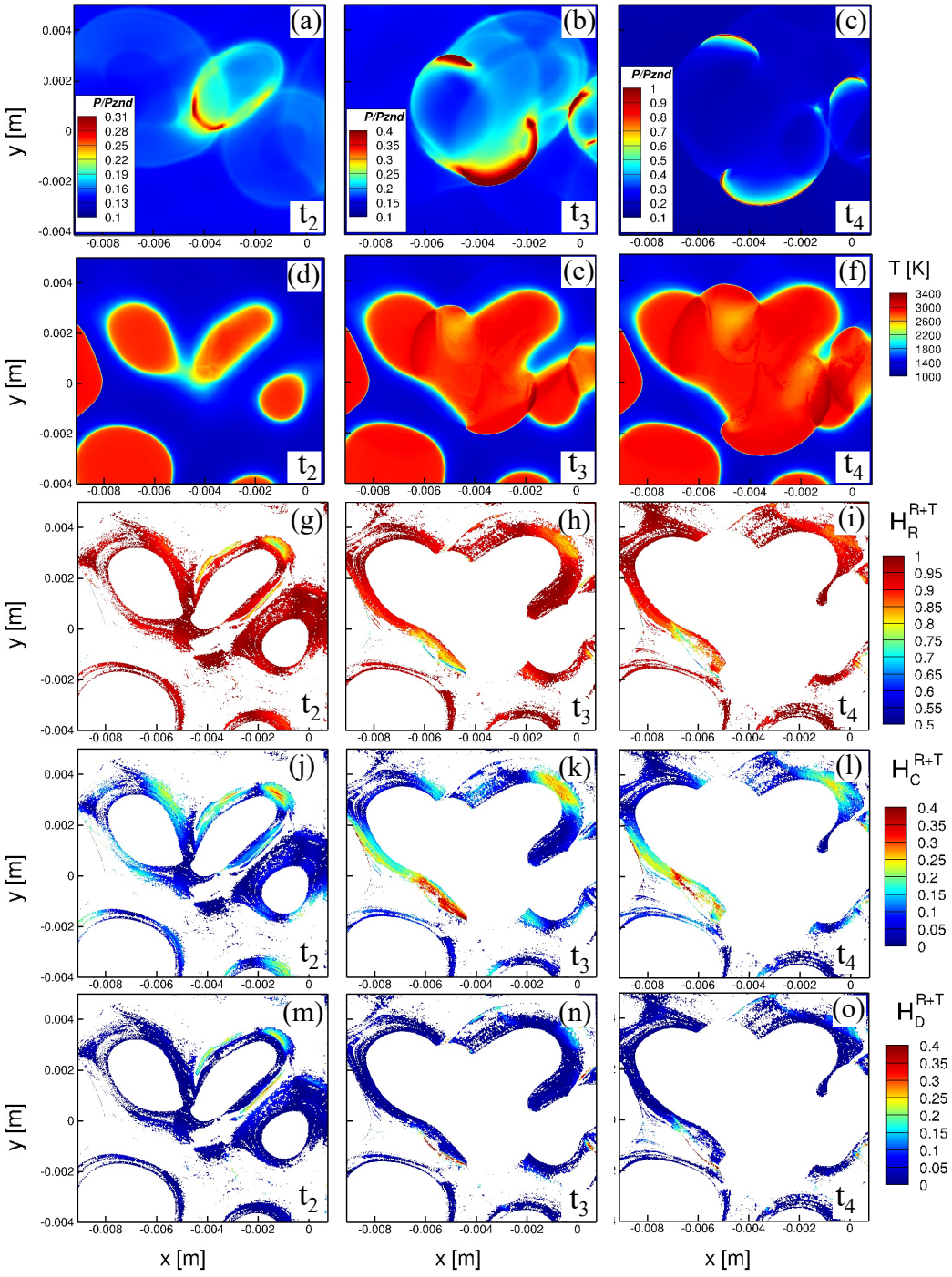

Figure 9. Pressure and temperature fields along with the spatial distributions of H_R^{R+T}, H_C^{R+T} and H_D^{R+T}, conditioned with $\Omega_{R+T} > 0$, for Case A at t_2 - t_4. The analysis focuses on the specific region where the detonation is developed.

All these findings consistently underscore the enhanced role of the transport processes (particularly convection) in the detonation development. However, since Fig. 8 shows the entire data points in the computational domain, a subsequent analysis is conducted by confining the observation near the region of the detonation development sites. Figure 9 displays the spatial distributions of pressure and temperature along with the H_R^{R+T}, H_C^{R+T} and H_D^{R+T}, conditioned to the areas where $\Omega_{R+T} > 0$, i.e. where detonation develops, at three different times, t_2, t_3 and t_4. The first notable finding is that the area where pressure

Preprints (www.preprints.org) | NOT PEER-REVIEWED | Posted: 27 May 2022 doi:10.20944/preprints202205.0377.v1

reaches high values at t_3 and t_4 is largely characterized by dissipative and not explosive dynamics. This is an important point to note, although it may not be surprising considering that the fuel is mostly consumed to yield the high temperature equilibrium state. In the meantime, the explosive dynamics is observed in the upstream of the periphery of the ignition fronts, with its magnitude decaying over time as the ignition fronts collide and merge.

Second, the explosive dynamics is largely characterized by the enhanced role of chemistry, as evidenced by the high values of H_R^{R+T}. However, transport processes (primarily convection) appear to have an increased role. In particular, even at the early stage of t_2, the locations of explosive dynamics exhibit increased values of H_C^{R+T}, which become magnified as time progresses. At t_3, some regions of explosive dynamics show the value of H_C^{R+T} exceeding 40%. By comparing with the pressure distribution, it is evident that this area is at the edge of the detonation front. In all cases, except for some small regions as seen in (j), the contribution of diffusive transport, H_D^{R+T}, is found to be much smaller. At t_4, after the detonation front is established, while the peak pressure behind the front reaches even higher values, the contribution of convection diminishes.

Note that the increased role of the transport processes manifested in Fig. 9 (and particularly that of convection, H_C^{R+T}) occurs at regions located at the edge of the localized pressure wave. This can be explained by considering that the temporal evolution of the localized pressure waves depends on the onset of ignition kernels which grow in space and eventually collide. The collision and interaction of the multiple ignition kernels (3 in the detonation event displayed in Fig. 9) and their associated ignition fronts leads to the increase of the amplitude of the localised pressure wave. Hence, the increased role of transport is highly associated with the augmented amplitude of localised pressure wave, i.e., a stronger pressure wave increases the role of transport that enhances the subsequent detonation development.

This finding is demonstrated both prior to the detonation onset, i.e., at t_2 and t_3 but also at t_4, i.e., when detonation has just started evolving. The established cause-and-effect relationship between detonation onset and the increased role of convection is a unique feature that may be utilized as an important observable for predicting detonation using the machine learning (ML) algorithm based on the data analysis; the role of convection, conditioned with explosive dynamics along with the Ω_{R+T}, would serve as features for the training algorithm.

To quantify the differences between the detonation development in Case A and the deflagration in Case B, a statistical analysis was performed by computing the averages of Ω_R, Ω_{R+T}, H_R^{R+T}, H_C^{R+T} and H_D^{R+T} conditioned against temperature, as the metric to indicate the explosive dynamics, i.e., either $\Omega_R>0$ or $\Omega_{R+T}>0$. For Case A, the statistical average was performed on the regions of detonation development only, as displayed in Fig. 9, while for Case B, the entire computational domain was considered. The results for times t_2, t_3 and t_4 are shown in Fig. 10. The rationale for the different averaging procedures between Cases A and B, was to isolate the physical characteristics pertinent to the detonation development, thereby allowing them to stand out in the comparison against non-detonating events (i.e., deflagration and autoignition). Since Case A includes both detonating and non-detonating events, averaging data from the whole domain would smooth out the features associated with the detonating events.

As for the main explosive features, Ω_R and Ω_{R+T}, Case A exhibits consistently higher level of explosiveness at all times and at medium to high temperatures where the detonation front forms. At low to medium temperatures, both Ω_R and Ω_{R+T} are comparable for Cases A and B. Consistent with the behavior seen in Fig. 7, these findings imply that stronger explosive dynamics associated with detonation is manifested in both Ω_R and Ω_{R+T}, although the latter exhibits more pronounced difference between Cases A and B, suggesting that the inclusion of transport component in predicting explosive dynamics is likely to result in better prediction. Therefore, the training of a ML algorithm in the progress variable space using Ω_R or Ω_{R+T} as features and data representative of deflagration

Preprints (www.preprints.org) | NOT PEER-REVIEWED | Posted: 27 May 2022 doi:10.20944/preprints202205.0377.v1

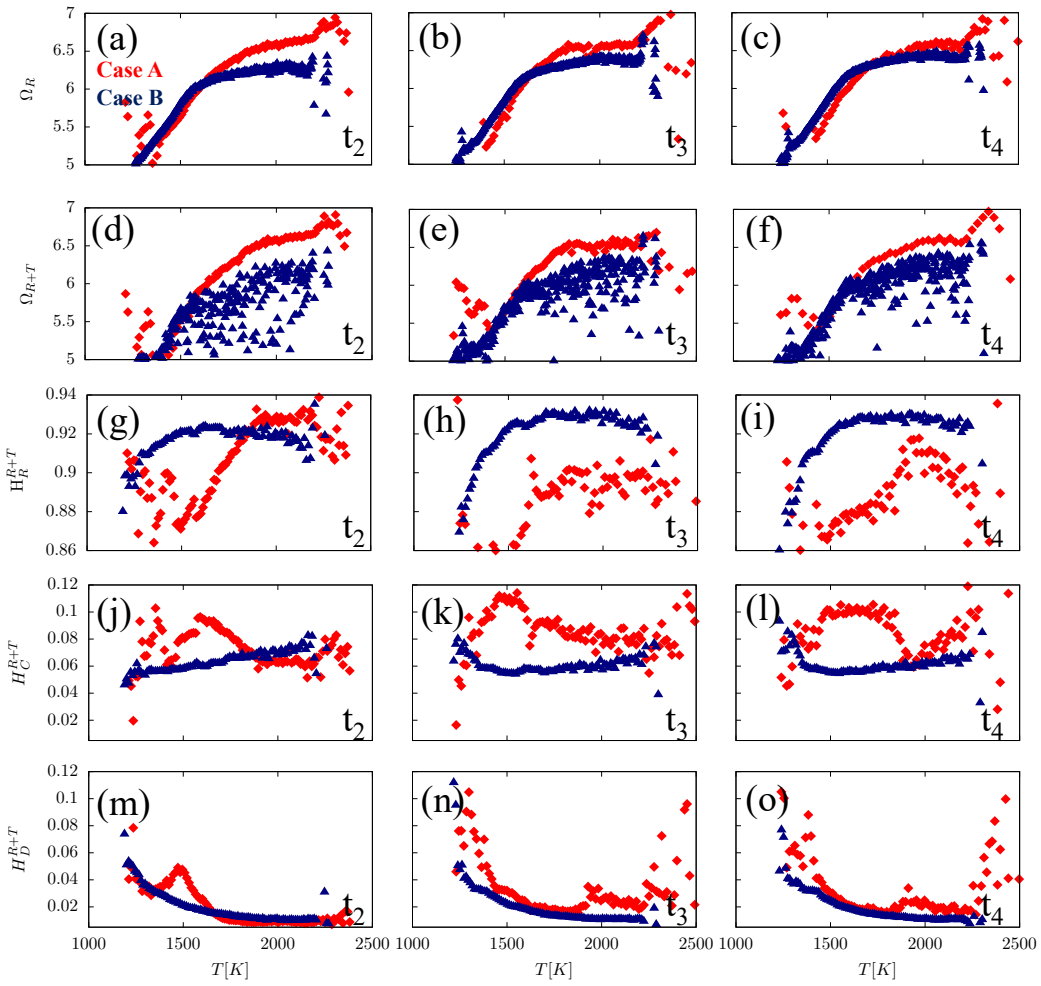

Figure 10. (a - c) Ω_R, (d - f) Ω_{R+T}, contributions of (g - i) chemical reactions, (j - l) convection, (m - o) diffusion to Ω_{R+T}, where Case A is denoted with red diamond symbols and for Case B blue triangles are used. The results for Case A are produced on the basis of the computational domain that detonation first develops, i.e., the computational domain illustrated in Fig. 9, while for Case B the whole computational domain. In both cases only the points characterized by explosive dynamics were considered ($\Omega_R>0$ or $\Omega_{R+T}>0$).

combustion mode, would be effective in allowing it to identify points in the physical space that are likely to develop detonation.

Figure 10 (g)-(o) reveals that the explosive dynamics of deflagration is primarily driven by chemical reactions, while for detonation the relative contribution of convection increases noticeably. For all cases at all times, the contributions from the diffusive transport to explosive dynamics remain small.

A further analysis of the individual indices revealed that the dominant process responsible for the increase in H_C^{R+T} in the detonating case is heat convection, and this serves as a main observable in detecting the detonation characteristics. This finding further corroborates the selection of H_C^{R+T} as a feature of a ML algorithm that will predict the occurrence of detonation events. As discussed earlier, however, the increased role of convection occurs at the edge of the detonating front and not at the main section, thereby suggesting that it is the outcome of the detonation development.

4. Conclusions

In the present study, two 2D high-fidelity numerical simulations were used as a parametric study to identify key differences in the dynamics of a detonating case against

deflagration, in view of asymptotic analysis. Advanced mathematical tools developed through the computational singular perturbation framework were used in order to: (i) identify the locations where the dynamics of the system becomes explosive and (ii) investigate the interplay between chemistry and transport processes. The analysis revealed that:

- the detonating case exhibited stronger explosive dynamics, as manifested both in the higher values obtained for the Ω_{R+T} metric and the wider region in the progress variable space that the dynamics became explosive. This finding suggests a more reactive state obtained for the detonation development.
- the contribution of the chemical reactions were largely the main force driving both the detonation and the deflagration cases.
- in the detonating case, the explosive dynamics was generally characterized by the enhanced role of convection, occurring at the edge of the detonating front.
- the enhanced role of convection in the detonating case was mainly due to heat convection.
- the dynamics of the main part of the detonating front was primarily characterized by dissipative and not explosive dynamics, since there the fuel was largely consumed and the temperature was very high.
- the role of diffusion was found to be insignificant in both examined cases.

We believe that the results proposed herein could assist in the design of effective machine learning algorithms which will predict the detonation onset at real-engine conditions.

Funding: This research received no external funding.

Informed Consent Statement: Not applicable.

Data Availability Statement: Not applicable.

Acknowledgments: This work was sponsored by King Abdullah University of Science and Technology (KAUST) and used the computational resources of the KAUST Supercomputing Laboratory.

Conflicts of Interest: The authors declare no conflict of interest.

References

1. Kalghatgi, G. Is it really the end of internal combustion engines and petroleum in transport? *Applied Energy* **2018**, *225*, 965–974. doi:10.1016/j.apenergy.2018.05.076.
2. Singh, E.; Tingas, E.A.; Goussis, D.; Im, H.G.; Sarathy, S.M. Chemical ignition characteristics of ethanol blending with primary reference fuels. *Energy & Fuels* **2019**, *33*, 10185–10196.
3. Kapusuz, M.; Cakmak, A.; Ozcan, H. Emissions analysis of an SI engine with humidified air induction. *Energy Procedia* **2018**, *147*, 235–241. doi:10.1016/j.egypro.2018.07.087.
4. Mohd Nawi, M.A.H.; Mohd Hanid, M.H.; Mustafa, W.A.; Kasim, M.S.; Raja Abdullah, R.I. Pollutant Emission in Diesel Engine. In *Intelligent Manufacturing and Mechatronics*; Jamaludin, Z.; Ali Mokhtar, M.N., Eds.; Springer Singapore: Singapore, 2020; pp. 288–298. Series Title: Lecture Notes in Mechanical Engineering, doi:10.1007/978-981-13-9539-0_29.
5. Khreis, H.; Niewenhuijsen, M.; Zietsman, J.; Ramani, T. *Traffic-Related Air Pollution*; Elsevier, 2020. doi:10.1016/C2018-0-02716-4.
6. Lorenzo, M.D.; Brequigny, P.; Foucher, F.; Mounaim-Rousselle, C. Turbulent Flame Speed of a Gasoline surrogate in conditions representative of modern downsized Spark-Ignition engine. *Combustion and Flame* **2022**, *240*, 112041. doi:10.1016/j.combustflame.2022.112041.
7. Baek, S.; Lee, H.; Lee, K. Fuel efficiency and exhaust characteristics of turbocharged diesel engine equipped with an electric supercharger. *Energy* **2021**, *214*, 119049. doi:10.1016/j.energy.2020.119049.
8. Wei, H.; Shao, A.; Hua, J.; Zhou, L.; Feng, D. Effects of applying a Miller cycle with split injection on engine performance and knock resistance in a downsized gasoline engine. *Fuel* **2018**, *214*, 98–107. doi:10.1016/j.fuel.2017.11.006.
9. Robert, A.; Richard, S.; Colin, O.; Poinsot, T. LES study of deflagration to detonation mechanisms in a downsized spark ignition engine. *Combustion and Flame* **2015**, *162*, 2788–2807. doi:10.1016/j.combustflame.2015.04.010.
10. Zhuang, Y.; Sun, Y.; Huang, Y.; Teng, Q.; He, B.; Chen, W.; Qian, Y. Investigation of water injection benefits on downsized boosted direct injection spark ignition engine. *Fuel* **2020**, *264*, 116765. doi:10.1016/j.fuel.2019.116765.
11. Zhao, X.; Zhu, Z.; Zheng, Z.; Yue, Z.; Wang, H.; Yao, M. Effects of flame propagation speed on knocking and knock-limited combustion in a downsized spark ignition engine. *Fuel* **2021**, *293*, 120407. doi:10.1016/j.fuel.2021.120407.
12. Wang, Y.; Wei, H.; Zhou, L.; Zhang, X.; Zhong, L. Effects of reactivity inhomogeneities on knock combustion in a downsized spark-ignition engine. *Fuel* **2020**, *278*, 118317. doi:10.1016/j.fuel.2020.118317.

13. Serrano, J.R.; Piqueras, P.; De la Morena, J.; Gómez-Vilanova, A.; Guilain, S. Methodological analysis of variable geometry turbine technology impact on the performance of highly downsized spark-ignition engines. *Energy* **2021**, *215*, 119122. doi:10.1016/j.energy.2020.119122.
14. Fraser, N.; Blaxill, H.; Lumsden, G.; Bassett, M. Challenges for Increased Efficiency through Gasoline Engine Downsizing. *SAE International Journal of Engines* **2009**, *2*, 991–1008. doi:10.4271/2009-01-1053.
15. López, J.J.; García, A.; Monsalve-Serrano, J.; Cogo, V.; Wittek, K. Potential of a two-stage variable compression ratio downsized spark ignition engine for passenger cars under different driving conditions. *Energy Conversion and Management* **2020**, *203*, 112251. doi:10.1016/j.enconman.2019.112251.
16. Wang, Z.; Qi, Y.; He, X.; Wang, J.; Shuai, S.; Law, C.K. Analysis of pre-ignition to super-knock: Hotspot-induced deflagration to detonation. *Fuel* **2015**, *144*, 222–227. doi:10.1016/j.fuel.2014.12.061.
17. Gautam T Kalghatgi.; Derek Bradley. Pre-ignition and 'super-knock' in turbo-charged spark-ignition engines. *Int. J. Engine Res.* **2012**, *13*, 399–414.
18. Morganti, K.; Abdullah, M.; Alzubail, A.; Viollet, Y.; Head, R.; Chang, J.; Kalghatgi, G. Improving the efficiency of conventional spark-ignition engines using octane-on-demand combustion-Part I: Engine Studies. *SAE technical paper* **2016**, pp. 01–0679.
19. Morganti, K.; Alzubail, A.; Abdullah, M.; Viollet, Y.; Head, R.; Chang, J.; Kalghatgi, G. Improving the efficiency of conventional spark-ignition engines using octane-on-demand combustion-Part II: vehicle studies and life cycle assessment. *SAE technical paper* **2016**, pp. 01–0683.
20. Chapman, E.M.; Costanzo, V.S. A literature review of abnormal ignition by fuel and lubricant derivatives. *SAE International Journal of Engines* **2016**, *9*, 107–142.
21. Kalghatgi, G.; Morganti, K.; Algunaibet, I.; Sarathy, M.; Dibble, R. Knock prediction using a simple model for ignition delay. *Shock* **2016**, *1*, 3.
22. Kalghatgi, G.T. Developments in internal combustion engines and implications for combustion science and future transport fuels. *Proc. Combust. Inst.* **2015**, *35*, 101–115.
23. Chen, L.; Li, T.; Yin, T.; Zheng, B. A predictive model for knock onset in spark-ignition engines with cooled EGR. *Energy Conversion and Management* **2014**, *87*, 946–955. doi:10.1016/j.enconman.2014.08.002.
24. Ze'ldovich, Y. Regime classification of an exothermic reaction with nonuniform initial conditions **1980**. *39*, 211–214.
25. Lee, J.H.S. *The Detonation Phenomenon*; 2008.
26. Wang, Z.; Liu, H.; Reitz, R.D. Knocking combustion in spark-ignition engines. *Progress in Energy and Combustion Science* **2017**, *61*, 78–112. doi:10.1016/j.pecs.2017.03.004.
27. Gong, Z.; Feng, L.; Wang, Z. Experimental and numerical study of the effect of injection strategy and intake valve lift on super-knock and engine performance in a boosted GDI engine. *Fuel* **2019**, *249*, 309–325. doi:10.1016/j.fuel.2019.03.005.
28. Dai, P.; Chen, Z. Effects of NOx addition on autoignition and detonation development in DME/air under engine-relevant conditions. *Proceedings of the Combustion Institute* **2019**, *37*, 4813–4820. doi:10.1016/j.proci.2018.06.063.
29. Liu, H.; Wang, Z.; Qi, Y.; He, X.; Wang, Y.; Wang, J. Super-knock suppression for highly turbocharged spark ignition engines using the fuel of propane or methanol. *Energy* **2019**, *169*, 1112–1118. doi:10.1016/j.energy.2018.12.058.
30. Mubarak Ali, M.J.; Hernandez Perez, F.; Vedharaj, S.; Vallinayagam, R.; Dibble, R.; Im, H. Effect of Timing and Location of Hotspot on Super Knock during Pre-ignition. 2017, pp. 2017–01–0686. doi:10.4271/2017-01-0686.
31. Dai, P.; Chen, Z.; Gan, X.; Liberman, M.A. Autoignition and detonation development from a hot spot inside a closed chamber: Effects of end wall reflection. *Proceedings of the Combustion Institute* **2021**, *38*, 5905–5913. doi:10.1016/j.proci.2020.09.025.
32. Zhou, L.; Kang, R.; Wei, H.; Feng, D.; Hua, J.; Pan, J.; Chen, R. Experimental analysis of super-knock occurrence based on a spark ignition engine with high compression ratio. *Energy* **2018**, *165*, 68–75. doi:10.1016/j.energy.2018.09.166.
33. Bradley, D.; Morley, C.; Gu, X.J.; Emerson, D.R. Amplified Pressure Waves During Autoignition: Relevance to CAI Engines. 2002, pp. 2002–01–2868. doi:10.4271/2002-01-2868.
34. Gu, X.; Emerson, D.; Bradley, D. Modes of reaction front propagation from hot spots. *Combust. Flame* **2003**, *133*, 63–74.
35. Bradley, D.; Kalghatgi, G. Influence of autoignition delay time characteristics of different fuels on pressure waves and knock in reciprocating engines. *Combustion and Flame* **2009**, *156*, 2307–2318. doi:10.1016/j.combustflame.2009.08.003.
36. Dai, P.; Chen, Z.; Chen, S.; Ju, Y. Numerical experiments on reaction front propagation in n-heptane/air mixture with temperature gradient. *Proc. Combust. Inst.* **2015**, *35*, 3045–3052.
37. Yu, H.; Chen, Z. End-gas autoignition and detonation development in a closed chamber. *Combust. Flame* **2015**, *162*, 4102–4111.
38. Qi, C.; Dai, P.; Yu, H.; Chen, Z. Different modes of reaction front propagation in n-heptane/air mixture with concentration non-uniformity. *Proc. Combust. Inst.* **2017**, *36*, 3633–3641.
39. Dai, P.; Qi, C.; Chen, Z. Effects of initial temperature on autoignition and detonation development in dimethyl ether/air mixtures with temperature gradient. *Proc. Combust. Inst.* **2017**, *36*, 3643–3650.
40. Chen, L.; Wei, H.; Chen, C.; Feng, D.; Zhou, L.; Pan, J. Numerical investigations on the effects of turbulence intensity on knocking combustion in a downsized gasoline engine. *Energy* **2019**, *166*, 318–325. doi:10.1016/j.energy.2018.10.058.
41. Su, J.; Dai, P.; Chen, Z. Detonation development from a hot spot in methane/air mixtures: Effects of kinetic models. *Int. J. Engine Res.* **2020**, p. 146808742094461. doi:https://doi.org/10.1177/1468087420944617.
42. Gao, Y.; Dai, P.; Chen, Z. Numerical studies on autoignition and detonation development from a hot spot in hydrogen/air mixtures. *Combustion Theory and Modelling* **2020**, *24*, 245–261.

43. Pan, J.; Wei, H.; Shu, G.; Chen, R. Effect of pressure wave disturbance on auto-ignition mode transition and knocking intensity under enclosed conditions. *Combust. Flame* **2017**, *185*, 63–74.
44. Pan, J.; Wei, H.; Shu, G.; Chen, Z.; Zhao, P. The role of low temperature chemistry in combustion mode development under elevated pressures. *Combust. Flame* **2016**, *174*, 179–193.
45. Terashima, H.; Matsugi, A.; Koshi, M. Origin and reactivity of hot-spots in end-gas autoignition with effects of negative temperature coefficients: Relevance to pressure wave developments. *Combust. Flame* **2017**, *184*, 324–334.
46. Sow, A.; Lee, B.J.; Hernández Pérez, F.E.; Im, H.G. Detonation onset in a thermally stratified constant volume reactor. *Proceedings of the Combustion Institute* **2019**, *37*, 3529–3536. doi:10.1016/j.proci.2018.08.043.
47. Luong, M.B.; Desai, S.; Hernández Pérez, F.E.; Sankaran, R.; Johansson, B.; Im, H.G. Effects of Turbulence and Temperature Fluctuations on Knock Development in an Ethanol/Air Mixture. *Flow, Turbulence and Combustion* **2021**, *106*, 575–595. doi:10.1007/s10494-020-00171-9.
48. Luong, M.B.; Im, H.G. Prediction of the developing detonation in an NTC-fuel/air mixture with temperature inhomogeneities under engine conditions. *Submitted to Proc. Combust. Inst.* **2022**.
49. Takens, F. Partially hyperbolic fixed points. *Topology* **1971**, *10*, 133–147.
50. Hirsch, M.P.; Pugh, C. C., Shub, M. Invariant manifolds. *Lect. Notes in Math* **1977**, *583*.
51. Fenichel, N. Geometric singular perturbation theory for ordinary differential equations. *Journal of differential equations* **1979**, *31*, 53–98.
52. Lam, S.H.; Goussis, D.A. Understanding complex chemical kinetics with computational singular perturbation. In Proceedings of the Symposium (International) on Combustion. Elsevier, 1989, Vol. 22, pp. 931–941.
53. Lam, S.; Goussis, D. Basic theory and demonstrations of computational singular perturbation for stiff equations. In Proceedings of the 12th IMACS World Congress on Scientific Computation, Paris, France, July, 1988, pp. 18–22.
54. Lam, S.H.; Coussis, D. Conventional asymptotics and computational singular perturbation for simplified kinetics modelling. In *Reduced kinetic mechanisms and asymptotic approximations for methane-air flames*; Springer, 1991; pp. 227–242.
55. Goussis, D.; Lam, S. A study of homogeneous methanol oxidation kinetics using CSP. In Proceedings of the Symposium (International) on Combustion. Elsevier, 1992, Vol. 24, pp. 113–120.
56. Lam, S.; Goussis, D. The CSP method for simplifying kinetics. *International journal of chemical kinetics* **1994**, *26*, 461–486.
57. Hadjinicolaou, M.; Goussis, D.A. Asymptotic solution of stiff PDEs with the CSP method: the reaction diffusion equation. *SIAM Journal on Scientific Computing* **1998**, *20*, 781–810.
58. Valorani, M.; Najm, H.N.; Goussis, D.A. CSP analysis of a transient flame-vortex interaction: time scales and manifolds. *Combustion and Flame* **2003**, *134*, 35–53.
59. Najm, H.N.; Valorani, M.; Goussis, D.A.; Prager, J. Analysis of methane–air edge flame structure. *Combustion Theory and Modelling* **2010**, *14*, 257–294.
60. Prager, J.; Najm, H.N.; Valorani, M.; Goussis, D. Structure of n-heptane/air triple flames in partially-premixed mixing layers. *Combustion and Flame* **2011**, *158*, 2128–2144.
61. Gupta, S.; Im, H.G.; Valorani, M. Analysis of n-heptane auto-ignition characteristics using computational singular perturbation. *Proceedings of the Combustion Institute* **2013**, *34*, 1125–1133.
62. Goussis, D.A.; Najm, H.N. Model reduction and physical understanding of slowly oscillating processes: the circadian cycle. *Multiscale Modeling & Simulation* **2006**, *5*, 1297–1332.
63. Kourdis, P.D.; Steuer, R.; Goussis, D.A. Physical understanding of complex multiscale biochemical models via algorithmic simplification: Glycolysis in Saccharomyces cerevisiae. *Physica D: Nonlinear Phenomena* **2010**, *239*, 1798–1817.
64. Kourdis, P.D.; Palasantza, A.G.; Goussis, D.A. Algorithmic asymptotic analysis of the NF-κB signaling system. *Computers & Mathematics with Applications* **2013**, *65*, 1516–1534.
65. Kourdis, P.D.; Goussis, D.A. Glycolysis in saccharomyces cerevisiae: algorithmic exploration of robustness and origin of oscillations. *Mathematical biosciences* **2013**, *243*, 190–214.
66. Patsatzis, D.G.; Goussis, D.A. A new Michaelis-Menten equation valid everywhere multi-scale dynamics prevails. *Mathematical biosciences* **2019**, *315*, 108220.
67. Patsatzis, D.G.; Tingas, E.A.; Goussis, D.A.; Sarathy, S.M. Computational singular perturbation analysis of brain lactate metabolism. *PloS one* **2019**, *14*, e0226094.
68. Patsatzis, D.; Tingas, E.A.; Sarathy, S.; Goussis, D.; Jolivet, R. Identification of Key Processes and Periods in a Model of Human Brain Energy Metabolism by Algorithmic Decomposition with Computational Singular Perturbation. In Proceedings of the GLIA. WILEY 111 RIVER ST, HOBOKEN 07030-5774, NJ USA, 2021, Vol. 69, pp. E236–E237.
69. Patsatzis, D.G.; Tingas, E.A.; Goussis, D.A.; Sarathy, S.M. Chemical Kinetics of Brain Metabolism: Equilibrations and Control of the Process. In Proceedings of the International Conference on Mathematics in (bio) Chemical Kinetics and Engineering, 2018.
70. Patsatzis, D.G.; Maris, D.T.; Goussis, D.A. Asymptotic analysis of a target-mediated drug disposition model: algorithmic and traditional approaches. *Bulletin of mathematical biology* **2016**, *78*, 1121–1161.
71. Michalaki, L.I.; Goussis, D.A. Asymptotic analysis of a TMDD model: when a reaction contributes to the destruction of its product. *Journal of mathematical biology* **2018**, *77*, 821–855.
72. Jaasim, M.; Tingas, E.A.; Pérez, F.E.H.; Im, H.G. Computational singular perturbation analysis of super-knock in SI engines. *Fuel* **2018**, *225*, 184–191.

73. Luong, M.B.; Hernández Pérez, F.E.; Im, H.G. Prediction of ignition modes of NTC-fuel/air mixtures with temperature and concentration fluctuations. *Combustion and Flame* **2020**, *213*, 382–393. doi:10.1016/j.combustflame.2019.12.002.
74. Luong, M.B.; Desai, S.; Hernández Pérez, F.E.; Sankaran, R.; Johansson, B.; Im, H.G. A statistical analysis of developing knock intensity in a mixture with temperature inhomogeneities. *Proceedings of the Combustion Institute* **2021**, *38*, 5781–5789. doi:10.1016/j.proci.2020.05.044.
75. Javed, T.; Badra, J.; Jaasim, M.; Es-Sebbar, E.; Labastida, M.F.; Chung, S.H.; Im, H.G.; Farooq, A. Shock Tube Ignition Delay Data Affected by Localized Ignition Phenomena. *Combustion Science and Technology* **2017**, *189*, 1138–1161. doi:10.1080/00102202.2016.1272599.
76. Senecal, P.K.; Pomraning, E.; Richards, K.J.; Briggs, T.E.; Choi, C.Y.; Mcdavid, R.M.; Patterson, M.A. Multi-Dimensional Modeling of Direct-Injection Diesel Spray Liquid Length and Flame Lift-off Length using CFD and Parallel Detailed Chemistry. 2003, pp. 2003–01–1043. doi:10.4271/2003-01-1043.
77. Bhagatwala, A.; Chen, J.H.; Lu, T. Direct numerical simulations of HCCI/SACI with ethanol. *Combustion and Flame* **2014**, *161*, 1826–1841. doi:10.1016/j.combustflame.2013.12.027.
78. Im, H.G.; Pal, P.; Wooldridge, M.S.; Mansfield, A.B. A Regime Diagram for Autoignition of Homogeneous Reactant Mixtures with Turbulent Velocity and Temperature Fluctuations. *Combust. Sci. Technol.* **2015**, *187*, 1263–1275.
79. Towery, C.A.Z.; Poludnenko, A.Y.; Hamlington, P.E. Detonation initiation by compressible turbulence thermodynamic fluctuations. *Combust. Flame* **2020**, *213*, 172–183.
80. Figueroa-Labastida, M.; Luong, M.B.; Badra, J.; Im, H.G.; Farooq, A. Experimental and computational studies of methanol and ethanolpreignition behind reflected shock waves. *Combust. Flame* **2021**, *234*, 111621.
81. Peters, N.; Kerschgens, B.; Paczko, G. Super-Knock Prediction Using a Refined Theory of Turbulence. *SAE Int. J. Engines* **2013**, *6*, 953–967.
82. Luong, M.B.; Im, H.G. Effects of low-temperature chemistry on detonation under engine-relevant conditions. *Accepted for oral presentation at the 39th International Symposium on Combustion.* **2022**.
83. Goussis, D.A.; Maas, U. Model reduction for combustion chemistry. In *Turbulent combustion modeling*; Springer, 2011; pp. 193–220.
84. Goussis, D.A. Quasi steady state and partial equilibrium approximations: their relation and their validity. *Combustion Theory and Modelling* **2012**, *16*, 869–926.
85. Goussis, D.A.; Im, H.G.; Najm, H.N.; Paolucci, S.; Valorani, M. The origin of CEMA and its relation to CSP. *Combustion and Flame* **2021**, *227*, 396–401.
86. Valorani, M.; Creta, F.; Ciottoli, P.P.; Malpica Galassi, R.; Goussis, D.; Najm, H.; Paolucci, S.; Im, H.G.; Tingas, E.A.; Manias, D.; et al. Computational singular perturbation method and tangential stretching rate analysis of large scale simulations of reactive flows: Feature tracking, time scale characterization, and cause/effect identification. Part 1, basic concepts. In *Data analysis for direct numerical simulations of turbulent combustion*; Springer, 2020; pp. 43–64.
87. Valorani, M.; Creta, F.; Ciottoli, P.P.; Malpica Galassi, R.; Goussis, D.; Najm, H.; Paolucci, S.; Im, H.G.; Tingas, E.A.; Manias, D.; et al. Computational Singular Perturbation Method and Tangential Stretching Rate Analysis of Large Scale Simulations of Reactive Flows: Feature Tracking, Time Scale Characterization, and Cause/Effect Identification. Part 2, Analyses of Ignition Systems, Laminar and Turbulent Flames. In *Data analysis for direct numerical simulations of turbulent combustion*; Springer, 2020; pp. 65–88.
88. Tingas, E.A.; Kyritsis, D.C.; Goussis, D.A. Autoignition dynamics of DME/air and EtOH/air homogeneous mixtures. *Combustion and Flame* **2015**, *162*, 3263–3276.
89. Tingas, E.A.; Manias, D.M.; Sarathy, S.M.; Goussis, D.A. CH4/air homogeneous autoignition: A comparison of two chemical kinetics mechanisms. *Fuel* **2018**, *223*, 74–85.
90. Manias, D.M.; Tingas, E.A.; Frouzakis, C.E.; Boulouchos, K.; Goussis, D.A. The mechanism by which CH2O and H2O2 additives affect the autoignition of CH4/air mixtures. *Combustion and Flame* **2016**, *164*, 111–125.
91. Li, Y.; Alfazazi, A.; Mohan, B.; Tingas, E.A.; Badra, J.; Im, H.G.; Sarathy, S.M. Development of a reduced four-component (toluene/n-heptane/iso-octane/ethanol) gasoline surrogate model. *Fuel* **2019**, *247*, 164–178.
92. Yalamanchi, K.K.; Tingas, E.A.; Im, H.G.; Sarathy, S.M. Screening gas-phase chemical kinetic models: Collision limit compliance and ultrafast timescales. *International Journal of Chemical Kinetics* **2020**, *52*, 599–610.
93. Tingas, E.A.; Kyritsis, D.C.; Goussis, D.A. H 2/air autoignition dynamics around the third explosion limit. *Journal of Energy Engineering* **2019**, *145*, 04018074.
94. Sharmin, N.; Tingas, E.A. Dynamics analysis of a jet-fuel surrogate and development of a skeletal mechanism for computational fluid dynamic applications. *Journal of Energy Engineering* **2020**, *146*, 04020064.
95. Tingas, E.A.; Kyritsis, D.C.; Goussis, D.A. Ignition delay control of DME/air and EtOH/air homogeneous autoignition with the use of various additives. *Fuel* **2016**, *169*, 15–24.
96. Tingas, E.A.; Wang, Z.; Sarathy, S.M.; Im, H.G.; Goussis, D.A. Chemical kinetic insights into the ignition dynamics of n-hexane. *Combustion and Flame* **2018**, *188*, 28–40.
97. Khalil, A.T.; Manias, D.M.; Tingas, E.A.; Kyritsis, D.C.; Goussis, D.A. Algorithmic analysis of chemical dynamics of the autoignition of NH3–H2O2/air mixtures. *Energies* **2019**, *12*, 4422.
98. Tingas, E.A.; Kyritsis, D.C.; Goussis, D.A. Comparative investigation of homogeneous autoignition of DME/air and EtOH/air mixtures at low initial temperatures. *Combustion Theory and Modelling* **2017**, *21*, 93–119.

99. Tingas, E.A. The chemical dynamics of hydrogen/hydrogen peroxide blends diluted with steam at compression ignition relevant conditions. *Fuel* **2021**, *296*, 120594.
100. Tingas, E.A. Computational analysis of the effect of hydrogen peroxide addition on premixed laminar hydrogen/air flames. *Fuel* **2021**, *302*, 121081.
101. Song, W.; Tingas, E.A.; Im, H.G. A computational analysis of methanol autoignition enhancement by dimethyl ether addition in a counterflow mixing layer. *Combustion and Flame* **2018**, *195*, 84–98.
102. Rabbani, S.; Manias, D.M.; Kyritsis, D.C.; Goussis, D.A. Chemical dynamics of the autoignition of near-stoichiometric and rich methanol/air mixtures. *Combustion Theory and Modelling* **2021**, pp. 1–31.
103. Manias, D.M.; Patsatzis, D.G.; Kyritsis, D.C.; Goussis, D.A. NH3 vs. CH4 autoignition: A comparison of chemical dynamics. *Combustion Theory and Modelling* **2021**, *25*, 1110–1131.
104. Khalil, A.T.; Manias, D.M.; Kyritsis, D.C.; Goussis, D.A. NO formation and autoignition dynamics during combustion of H2O-diluted NH3/H2O2 mixtures with air. *Energies* **2021**, *14*, 84.
105. Adrover, A.; Creta, F.; Giona, M.; Valorani, M. Stretching-based diagnostics and reduction of chemical kinetic models with diffusion. *Journal of Computational Physics* **2007**, *225*, 1442–1471.
106. Valorani, M.; Paolucci, S.; Martelli, E.; Grenga, T.; Ciottoli, P.P. Dynamical system analysis of ignition phenomena using the tangential stretching rate concept. *Combustion and Flame* **2015**, *162*, 2963–2990.
107. Valorani, M.; Ciottoli, P.P.; Galassi, R.M. Tangential stretching rate (TSR) analysis of non premixed reactive flows. *Proceedings of the Combustion Institute* **2017**, *36*, 1357–1367.
108. Ciottoli, P.P.; Lee, B.J.; Lapenna, P.E.; Galassi, R.M.; Hernández-Pérez, F.E.; Martelli, E.; Valorani, M.; Im, H.G. Large Eddy Simulation on the Effects of Pressure on Syngas/Air Turbulent Nonpremixed Jet Flames. *Combustion Science and Technology* **2020**, *192*, 1963–1996. doi:10.1080/00102202.2019.1632300.
109. Manias, D.M.; Tingas, E.A.; Minamoto, Y.; Im, H.G. Topological and chemical characteristics of turbulent flames at MILD conditions. *Combustion and Flame* **2019**, *208*, 86–98.
110. Manias, D.M.; Tingas, E.A.; Pérez, F.E.H.; Galassi, R.M.; Ciottoli, P.P.; Valorani, M.; Im, H.G. Investigation of the turbulent flame structure and topology at different Karlovitz numbers using the tangential stretching rate index. *Combustion and Flame* **2019**, *200*, 155–167.
111. Ciottoli, P.P.; Galassi, R.M.; Lapenna, P.E.; Leccese, G.; Bianchi, D.; Nasuti, F.; Creta, F.; Valorani, M. CSP-based chemical kinetics mechanisms simplification strategy for non-premixed combustion: An application to hybrid rocket propulsion. *Combustion and Flame* **2017**, *186*, 83–93.
112. Galassi, R.M. PyCSP: A Python package for the analysis and simplification of chemically reacting systems based on Computational Singular Perturbation. *Computer Physics Communications* **2022**, *276*, 108364.
113. Safta, C.; Najm, H.N.; Knio, O. TChem-a software toolkit for the analysis of complex kinetic models. Technical report, Sandia National Lab.(SNL-CA), Livermore, CA (United States), 2011.
114. Wang, Z.; Liu, H.; Song, T.; Qi, Y.; He, X.; Shuai, S.; Wang, J. Relationship between super-knock and pre-ignition. *International Journal of Engine Research* **2015**, *16*, 166–180. doi:10.1177/1468087414530388.
115. Farjam, S.; Savard, B. Ignition and flame stabilization of n-dodecane turbulent premixed flames under Spray A thermochemical conditions. *Combustion and Flame* **2022**, *242*, 112133.
116. Guo, H.; Xu, Y.; Li, S.; Zhang, H. On the evolutions of induction zone structure in wedge-stabilized oblique detonation with water mist flows. *Combustion and Flame* **2022**, *241*, 112122.
117. Huang, Z.; Cleary, M.J.; Ren, Z.; Zhang, H. Large eddy simulation of a supersonic lifted hydrogen flame with sparse-Lagrangian multiple mapping conditioning approach. *Combustion and Flame* **2022**, *238*, 111756.
118. Kim, J.H.; Yu, G.H.; Chung, S.H.; Yoo, C.S. A DNS study of ignition characteristics of a lean PRF/air mixture with CH2O and H2O2 addition under HCCI combustion-relevant conditions. *Combustion and Flame* **2021**, *234*, 111654.
119. Zhang, Z.; Abdelsamie, A.; Chi, C.; Thevenin, D.; Luo, K.H. Combustion Mode and Mixing Characteristics of a Reacting Jet in Crossflow. *Energy & Fuels* **2021**, *35*, 13325–13337.
120. Wang, H.; Wang, Z.; Luo, K.; Hawkes, E.R.; Chen, J.H.; Fan, J. Direct numerical simulation of turbulent boundary layer premixed combustion under auto-ignitive conditions. *Combustion and Flame* **2021**, *228*, 292–301.
121. Zhao, M.; Ren, Z.; Zhang, H. Pulsating detonative combustion in n-heptane/air mixtures under off-stoichiometric conditions. *Combustion and Flame* **2021**, *226*, 285–301.
122. Krisman, A.; Meagher, P.; Zhao, X.; Park, J.W.; Lu, T.; Chen, J.H. A direct numerical simulation of Jet A flame kernel quenching. *Combustion and Flame* **2021**, *225*, 349–363.
123. Manias, D.M.; Tingas, A.E.; Im, H.G.; Minamoto, Y. Dynamics analysis of a turbulent methane flame in mild combustion conditions. In Proceedings of the AIAA Scitech 2019 Forum, 2019, p. 1731.
124. Manias, D.; Tingas, A.E.; Hernandez Perez, F.E.; Im, H.G.; Galassi, R.M.; Ciottoli, P.P.; Valorani, M. Analysis of hydrogen/air turbulent premixed flames at different karlovitz numbers using computational singular perturbation. In Proceedings of the 2018 AIAA Aerospace Sciences Meeting, 2018, p. 0364.